Energy-Efficient Design and Control of a Vibro-Driven Robot

Pengcheng Liu, Gerhard Neumann, Qinbing Fu, Simon Pearson and Hongnian Yu

***Abstract* — Vibro-driven robotic (VDR) systems use stick-slip motions for locomotion. Due to the underactuated nature of the system, efficient design and control are still open problems. We present a new energy preserving design based on a spring-augmented pendulum. We indirectly control the friction-induced stick-slip motions by exploiting the passive dynamics in order to achieve an improvement in overall travelling distance and energy efficiency. Both collocated and non-collocated constraint conditions are elaborately analysed and considered to obtain a desired trajectory generation profile. For tracking control, we develop a partial feedback controller for the driving pendulum which counter-acts the dynamic contributions from the platform. Comparative simulation studies show the effectiveness and intriguing performance of the proposed approach, while its feasibility is experimentally verified through a physical robot. Our robot is to the best of our knowledge the first nonlinear-motion prototype in literature towards the VDR systems.**

I. Introduction

Motion generation schemes determine the capabilities, energy consumption and degrees of autonomy of miniature robotic systems. Many methods have been designed via mimicking earth-worm progression [1], canoe paddling [2], and magnetic field [3], [4], which have complex mechanism structures and therefore render motion control a challenging task. VDR systems [5]–[9] typically generate locomotion using interactions of internal impact force and external static friction, also called stick-slip motions. A rectilinear motion of the robot can be obtained through a mass/inertia internally interacting with the main body and overcoming resistance forces. Motion control problem of the VDR systems poses considerable challenges due to stringent kinematic and environment constraints in the presence of underactuated dynamics. The number of independent control inputs is typically less than the number of DOF to be controlled [10]. This reduction in actuators lowers the cost and increase the energy efficiency. However, describing and characterizing the performance of passive subsystems due to internal dynamics and couplings is challenging [11]. Therefore, it is necessary to consider dynamics of the nonholonomic constraints when designing the control systems. As such, the stick-slip effects can be effectively characterized to manipulate the locomotion of the VDR system as a whole.

Primary objectives for motion generation of VDR systems include the optimal travel distances, travel speeds and energy efficiency. Most of reported studies on trajectory planning of VDR systems mainly focus on optimization of trajectory parameters, as such, the maximal average velocity can be obtained. A mobile VDR system was studied in [12] that uses compliant tensegrity structures and one actuator for locomotion. Yu et al. designed a four-step acceleration-based control mode for a capsule-type VDR robot in [13]. Fang and Xu analysed the stick-slip effects of an internally controlled mass in [9] to optimally select the system parameters to improve performance in average velocity of the system. In that sense, friction and environment constraints play important roles in the locomotion of VDR systems. However, the majority of the reported studies concentrated either on the structural design for motion diversity [12] or on constraints analysis in the slow motion stage [14].

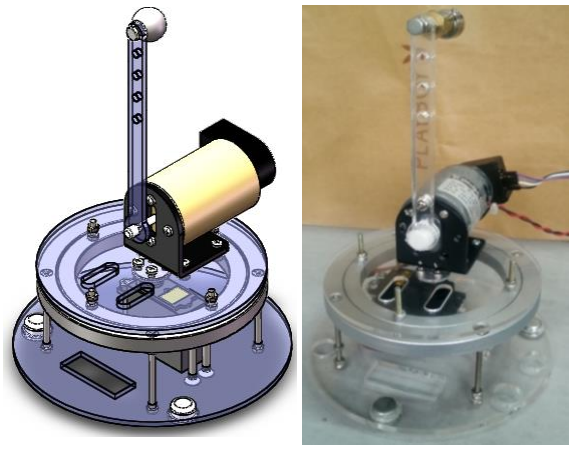

Fig. 1. The underactuated VDR system: the 3D model (left) and the physical robot prototype (right).

Instead, based on our previous work [5], this paper aims to control the motion and improve the energy efficiency of the VDR system by leveraging from the passive dynamics of a spring-augmented pendulum. The contributions of this paper are listed as follows: (1) We derive the system dynamics model and consider an inertia-spring-damper impedance model. (2) We present the first physical robotic prototype (as shown in Fig. 1) for VDR systems utilizing nonlinear motions. (3) To control the stick-slip motion of the VDR system, we design a desired trajectory for the pendulum using analytical design choices and dynamic constraint conditions. (4) We develop a partial feedback controller which drives the pendulum along the given desired trajectory, counteracting the dynamic contributions from the platform.

This paper is organized as follows. Section II presents the dynamic model of the underactuated VDR system. Section III develops a desired trajectory generation profile for the actuated subsystem. Section IV computes the parameters of the trajectory, and Section V proposes a tracking control scheme. Comparative simulation and experimental studies are

P. Liu, G. Neumann and Q. Fu ({pliu, gneumann, qifu}@lincoln.ac.uk) are with the Lincoln Centre for Autonomous Systems (L-CAS), University of Lincoln, Lincoln LN6 7TS, United Kingdom.

P. Liu and S. Pearson (spearson@lincoln.ac.uk) are with the Lincoln Institute for Agri-Food Technology (LIAT), University of Lincoln, Lincoln LN6 7TS, United Kingdom.

H. Yu (yuh@bournemouth.ac.uk) is with the Faculty of Science and Technology, Bournemouth University, Poole BH12 5BB, United Kingdom.

conducted in Sections VI and VII. Finally, concluding remarks and discussions are given in Section VIII.

II. Dynamics and Preliminaries

A. The Mathematical Model

TABLE I. PARAMETERS OF THE SYSTEM

Symbols	Description
θ (rad)	Angular displacement of the pendulum from vertical
x (cm)	Displacement of the platform from initial position
M (kg)	Mass of the platform
m (kg)	Mass of the pendulum (including the mass ball)
l (m)	Length of the inverted pendulum
μ (N/ms)	Coefficient of the friction
k (Nm/rad)	Elastic coefficient of the torsional spring
c $(kgm^2/srad)$	Coefficient of the viscous damper
f_c (N)	Horizontal sliding friction
f_0 (N)	The static friction force at zero motion speed
F_y (N)	Internal reaction forces in the vertical direction
u (Nm)	Control torque applied to the pendulum
g (m/s^2)	Gravitational acceleration
ω (rad/s)	Frequency of the excitation
θ_0 (rad)	Desired angular displacement of the pendulum

A schematic of the underactuated VDR model is given in Fig. 2, which shows a rotating pendulum and a sliding platform. An actuator is mounted at the pivot to rotate the pendulum. The interaction between actuator and pendulum is implemented via an inertia-spring-damper impedance model, which contains a torsional spring and a viscous damper. Parameters of the system are defined in Table I. The robotic platform is propelled over a surface rectilinearly via the interaction between driving forces and the horizontal sliding friction, resulting into an alternative sticking and slipping locomotion. Meanwhile, the elastic potential energy is stored and released alternatingly and synchronized with the contraction and relaxation of the torsional spring. The motion of the platform starts in a static state, and the robot moves when the resultant force applied on robot's body in the horizontal direction exceeds the frictional force. In the sticking phase, the resultant force applied on the robot's body in horizontal direction is less than the maximal static friction force. In the slipping phase, the resulting force is larger than the maximal static friction force. When this condition is met, the motion switches from sticking phase to slipping phase and the robot starts to move. The dynamics of the underactuated VDR system can be derived as

$$M(q)\ddot{q} + C(q,\dot{q})\dot{q} + K(q)q + G(q) + F_d = Bu, \quad (1)$$

where $q(t) = [\theta\ x]^T$ represents the system's configuration vector, $M(q) \in \mathcal{R}^{2\times2}$ is the inertia matrix, $C(q,\dot{q}) \in \mathcal{R}^{2\times2}$ is the Centripetal-Coriolis matrix, $K(q) \in \mathcal{R}^{2\times2}$ is the generalized stiffness matrix, $G(q) \in \mathcal{R}^{2\times1}$ represents the gravitational torques, $B \in \mathcal{R}^{2\times1}$ is the control input vector, $F_d(t)$ denotes the frictional forces, $u \in \mathcal{R}^1$ denotes the control input torque. Details of the variables are listed as

$$M(q) = \begin{bmatrix} ml^2 & -ml\cos\theta \\ -ml\cos\theta & (M+m) \end{bmatrix}, C(q,\dot{q}) = \begin{bmatrix} 0 & 0 \\ ml\sin\theta\dot{\theta} & 0 \end{bmatrix},$$

$$K(q) = \begin{bmatrix} k & 0 \\ 0 & 0 \end{bmatrix}, G(q) = [-mgl\sin\theta\ 0]^T,$$

$$B = [1\ 0]^T \text{ and } F_d(t) = [c\dot{\theta}\ f_c]^T.$$

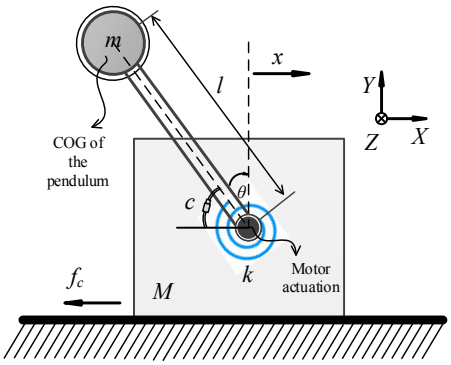

Fig. 2. Schematic of the underactuated VDR model.

It is noted that we assume the frictional dynamics are based on the Coulomb model, given as

$$f_c = \begin{cases} \mu(Mg + F_y)Sgn(\dot{x}), & for\ \dot{x} \neq 0\ , \\ f_0, & for\ \dot{x} = 0\ . \end{cases}$$

III. Trajectory Generation for the Actuated Subsystem

In our model, the harmonic property is introduced by an impedance model. System performance is largely determined by the counterbalance between rising and falling edges of the harmonic force [15]. For each motion cycle, the displacement obtained in the forward motion stage is partially counteracted by the following backward motion causing a sub-optimal energy efficiency. Thus, a two-stage trajectory profile is developed to obtain the desired objectives that uses harmonic ramping edges in the forward motion stage and sufficiently neutralizes backward motions triggered by the falling edges.

The trajectory is composed of the locomotion and restoring stages. In the locomotion stage, the pendulum is driven with high acceleration using the release of elastic energy stored in the torsional spring. The excitation frequency of the harmonic force is considered in this stage to synchronize the pendulum motion with the ramping edge. The resultant interaction force generates a slipping motion ($\dot{x} \neq 0$). In the restoring stage, the pendulum is carefully returned to the initial position, and potential energy is simultaneously stored in the torsional spring for the next motion cycle. The resultant interaction force in the horizontal direction is less than the maximum dry friction force, i.e., the robot remains in the sticking phase in this stage ($\dot{x} = 0$).

Considering the practical control index and dynamic constraints of the VDR system, the following design choices are proposed for the desired trajectory profile of the driving pendulum: (i) For each motion cycle, the pendulum is constrained rotating within an advisable angle range, indicating that upper and lower boundaries can be given as $|\theta(t)| \leq \theta_0$; (ii) The angular velocity and angular acceleration of the pendulum need to be placed within bounded ranges, i.e., $|\dot{\theta}(t)| \leq v_\theta$, $|\ddot{\theta}(t)| \leq a_\theta$; (iii) To maintain a non-bouncing motion of the robot, the contact force in the vertical direction has to be always greater than zero, i.e., $(M+m)g - ml\dot{\theta}^2cos\theta - ml\ddot{\theta}sin\theta - (k\theta + c\dot{\theta})sin\theta > 0$; (iv) In the restoring stage, the robot should keep stationary and wait for the pendulum to return to its initial positions. Hence, the force

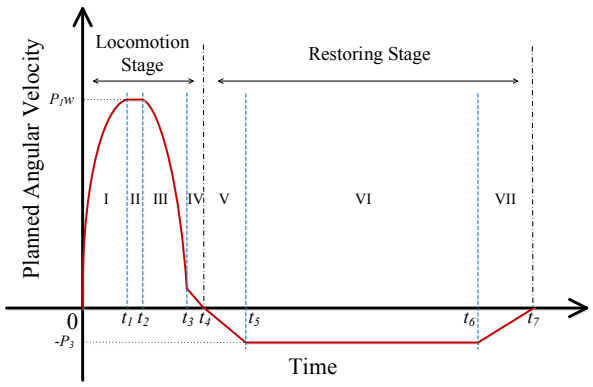

Fig. 3. Schematic profile for the angular velocity trajectory.

TABLE II. PARAMETERS OF THE TRAJECTORY

Symbols	Description
ν_θ (*rad/s*)	Absolute boundary of the angular velocity
a_θ (rad/s^2)	Absolute boundary of the angular acceleration
$P_1 * \omega$ (*rad/s*)	Upper boundary of the designed trajectory
P_2 (*rad/s*)	Critical boundary when the robot keeps stationary
P_3 (*rad/s*)	Lower boundary of the designed trajectory
t_1, t_1, …, t_7 (s)	Time durations from phase I to phase VII

of the driving pendulum applied on the robot in the horizontal direction needs to be less than the maximal static friction, i.e.,

$$\left|ml\ddot{\theta}cos\theta - ml\dot{\theta}^2sin\theta + (k\theta + c\dot{\theta})cos\theta\right| \le \mu[(M + m)g - ml\dot{\theta}^2cos\theta - ml\ddot{\theta}sin\theta - (k\theta + c\dot{\theta})sin\theta].$$

Consider the design choices above, Fig. 3 portrays the desired velocity profile which is designed for the actuated subsystem. The trajectory profile is mathmatically described in Eq. (2) and the trajectory parameters are listed in Table II. Detailed motion descriptions please refer to [16].

$$\dot{\theta}_d(t) = \begin{cases} P_1\omega sin\omega t, & t \in [0, t_1) \\ P_1\omega, & t \in [t_1, t_2) \\ P_1\omega \sin(\omega t - t_2), & t \in [t_2, t_3) \\ \frac{t_3 - t}{t_3 - t_2}P_2, & t \in [t_3, t_4) \\ \frac{t_3 - t}{t_4 - t_3}P_3, & t \in [t_4, t_5) \\ -P_3, & t \in [t_5, t_6) \\ \frac{t_6 - t}{t_5 - t_6}P_3, & t \in [t_6, t_7) \end{cases} \quad (2)$$

IV. TRAJECTORY PARAMETERIZATION

Here, to generate an efficient nominal forced trajectory, we take into consideration of the design choices. Firstly, environment constraint conditions are analysed to characterize the stick-slip motions. Analysis of the constraint condition for the complete robotic motion (time duration 0-t_7). Based on the design choice (iii), locomotion of the VDR system is on the sliding surface and no bouncing motion is allowed during the complete motion cycle, we have

$$\left(ml\ddot{\theta} + k\theta + c\dot{\theta}\right)sin\theta + ml\dot{\theta}^2cos\theta < (M + m)g.$$

This constraint can be achieved if the computed condition $\dot{\theta}^2\left|ml\ddot{\theta} + k\theta + c\dot{\theta}\right| < \varpi^2/2$ (with $\varpi = (M + m)g/\sqrt{ml}$) is satisfied.

Analysis of the constraint condition for the restoring stage (time duration t_3-t_7). Based on the design choice (iv), the robot keeps stationary in this stage. We consider the forces in horizontal and vertical directions and take one side of the inequality, we have

$$ml\ddot{\theta}cos\theta - ml\dot{\theta}^2sin\theta + (k\theta + c\dot{\theta})cos\theta \le \mu[(M + m)g - ml\dot{\theta}^2cos\theta - ml\ddot{\theta}sin\theta - (k\theta + c\dot{\theta})sin\theta].$$

This constraint can be achieved if the computed condition $\ddot{\theta} + \dot{\theta}^2 + k\theta + c\dot{\theta} \le \varpi'\vartheta$ (with $\varpi' = (M + m)g/ml, \vartheta = \mu/\sqrt{\mu^2 + 1}$) is satisfied. Then, the boundary conditions are defined to compute trajectory boundaries as $\dot{x}(t)_{|t=t_0,t_3,t_7} = 0, \theta(t)_{|t=t_0,t_7} = -\theta_0, \theta(t)_{|t=t_3} = \theta_0, \dot{\theta}(t)_{|t=t_0} = 0$.

To compute the critical boundary when the robot keeps stationary, we integrate the robot dynamics in Eq. (1) once along one complete motion cycle. In the duration $[0, t_3]$, P_2 can be obtained under the condition $mlcos\theta_0 + \mu mlsin\theta_0 \neq 0$, we have

$$P_2 = \dot{\theta}(t)_{|t=t_3} = \frac{1}{mlcos\theta_0 + \mu mlsin\theta_0}[\mu(M + m)gt_3 - \mu k\int_0^{t_3}\theta sin\theta dt + \mu c(\theta sin\theta - \int_0^{t_3}\theta cos\theta dt)].$$

Furthermore, the correlation between the upper, lower and critical trajectory boundaries can be obtained based on the principle of energy conservation in Fig. 3. Therefore, we have

$$\int_0^{t_1} P_1\omega_1 sin\omega t dt + P_1\omega_1(t_2 - t_1) + \int_{t_2}^{t_3} P_1\omega_1 \sin(\omega_1 t - t_2)dt - \frac{1}{2}P_2[\frac{N\pi}{\omega_1} + t_2 - t_3] = 2\theta_0,$$

$$-P_3[(t_7 - t_4) + (t_6 - t_5)] = P_2(t_4 - t_3) + 4\theta_0.$$

Computing time duration distributions for phase I and phase II: Applying the constraint condition for one complete robotic motion, we have

$$\dot{\theta}^2(t)_{|t=t_1}\left|ml\ddot{\theta}(t)_{|t=t_1} + k\theta(t)_{|t=t_1} + c\dot{\theta}(t)_{|t=t_1}\right| < \varpi^2/2$$

where $\dot{\theta}(t_1) = P_1\omega$, $\ddot{\theta}(t_1) = 0$ and $\theta(t_1) = P_1\omega t_1$. As a result, the upper boundary of Phase I can be yielded as

$$t_1 = \frac{1}{k}[\frac{\varpi^2}{2(P_1\omega)^3} - c]. \quad (3)$$

In this regard, we obtain a formulation for Phase II which is described by $P_1\omega\sin(\omega t_3 - t_2) = P_2$. Accordingly, the time duration distribution for phase II is computed as

$$t_2 = \omega t_3 - arcsin(P_2/P_1\omega). \quad (4)$$

Computing time duration distributions from phase III to phase V**:** The trajectory is designed to reach the amplitude of harmonic excitation at time t_1 and keep it till time t_2, gives

$$t_3 = N\pi/\omega_1. \quad (5)$$

During this period, the VDR system keeps stationary and allows a returning motion of the pendulum. Applying the constraint condition for the restoring stage, we have

$$\ddot{\theta}(t)_{|t=t_3,t_5} + \dot{\theta}(t)^2_{|t=t_3,t_5} + k\theta(t)_{|t=t_3,t_5} + c\dot{\theta}(t)_{|t=t_3,t_5} \le \varpi'\vartheta$$

where $\theta(t_3) = P_2t_3$, $\dot{\theta}(t_3) = P_2$, $\ddot{\theta}(t_3) = -P_2/(t_4 - t_3)$; and $\ddot{\theta}(t_5) = 0, \dot{\theta}(t_5) = P_3, \theta(t_5) = P_3t_5$.

Thereafter, the upper boundaries for time duration distributions of Phases IV and V can be given as

$$t_4 = -P_2/(\varpi'\vartheta - {P_2}^2 - kP_2t_3 - cP_2) + t_3, \quad (6)$$

$$t_5 = (\varpi'\vartheta - {P_3}^2 - cP_3)/kP_3. \quad (7)$$

Computing time duration distributions for phase VI and phase VII**:** From Fig. 3, the correlation between Phases IV, V and Phases VI, VII can be formulated as $P_2(t_5 - t_4) = P_3(t_4 - t_3)$. Therefore, related duration distributions can be obtained through combination with P_2, we have

$$t_6 = \frac{1}{2P_3}[4\theta_0 + t_4(P_2 + 2P_3) - P_2t_3], \quad (8)$$

$$t_7 = \frac{1}{2P_3}(4\theta_0 - P_2t_3 + P_2t_4 + 2P_3t_5). \quad (9)$$

V. Tracking Controller Design

In this section, to verify the performance of the VDR system and to make convenient comparisons with other approaches, a closed-loop feedback control scheme is developed. Based on the dynamic robotic model in Eq. (1) and after some calculations, we have

$$ml^2\left(1 - \frac{mcos^2\theta}{M+m}\right)\ddot{\theta} + \frac{1}{M+m}\left[mlc_\theta(mlsin\theta\dot{\theta}^2 + f)\right] - mglsin\theta + k\theta + c\dot{\theta} = u. \quad (10)$$

In the introduction, we stated that the underactuated VDR system is not completely feedback linearizable. Instead, we attempt to linearize a portion of the system dynamics. The dynamics of the robot are affected by motions of the driving pendulum. Therefore, it is reasonable that we create a feedback controller which drives the pendulum in exactly the way necessary to counter-act the dynamic contributions from the platform. By doing so, the dynamics of the platform can be linearized. The trajectory tracking error and its derivatives are defined as $\tilde{\theta} = \theta - \theta_d$, $\dot{\tilde{\theta}} = \dot{\theta} - \dot{\theta}_d$ and $\ddot{\tilde{\theta}} = \ddot{\theta} - \ddot{\theta}_d$.

Sustituting the tracking errors above into Eq. (10) and after appropriate mathematical manipulation, we arrive at the following system error dynamics

$$ml^2\left(1 - \frac{mc_\theta^2}{M+m}\right)\ddot{\tilde{\theta}} = u - \frac{[mlc_\theta(mlsin\theta\dot{\theta}^2+f)]}{M+m} + mglsin\theta - k\theta - c\dot{\theta} - ml^2\left(1 - \frac{mc_\theta^2}{M+m}\right)\ddot{\theta}_d. \quad (11)$$

Thus, a feedback linearizing controller can be designed from Eq. (11) using partial feedback linearization, we have

$$u = ml^2\left(1 - \frac{mc_\theta^2}{M+m}\right)\ddot{\theta}_d + \frac{[mlc_\theta(mls_\theta\dot{\theta}^2+f)]}{M+m} - mgls_\theta + k\theta + c\dot{\theta} - K_vml^2\left(1 - \frac{mc_\theta^2}{M+m}\right)\tilde{\theta} - K_pml^2\left(1 - \frac{m\cos^2\theta}{M+m}\right)\dot{\tilde{\theta}}. \quad (12)$$

where K_v and K_p are positive control gains selected by the designer. Substituting the tracking controller of Eq. (12) into error dynamics of Eq. (11), the closed-loop system can be obtained in Eq. (13). And the system stability can be guaranteed through the Routh-Hurwitz criterion.

$$\ddot{\tilde{\theta}} + K_v\dot{\tilde{\theta}} + K_p\tilde{\theta} = 0. \quad (13)$$

VI. Simulation Studies

Comparative simulation studies are conducted to verify the effectiveness of the inertia-spring-damper impedance model and motion generation apporach. In the simulation, system parameters are configured as reported in [14], [17] as $M = 0.5\,kg$, $m = 0.138\,kg$, $l = 0.3\,m$, $g = 9.81\,m/s^2$, $\mu = 0.01\,N/ms$ and natural frequency $\omega_n = 5.7184\,rad/s$. The control parameters are configured based on our previous studies one optimal selection of viscoelastic parameters in [15] as $k = 0.36\,Nm/rad$ and $c = 0.0923\,kgm^2/srad$ to maintain a locally optimal motion. Initial conditions are set as $\theta(0) = \theta_0 = \pi/3$, $\dot{\theta}(0) = 0$, $x(0) = 0$ and $\dot{x}(0) = 0$.

A. Verification of the Impedance Model

The introduction of energy storage mechanism in the VDR model is plausible to improve the energy efficiency. We verify the effectiveness of the impedance model through comparing to a VDR cart-pole system [14], which does not feature this design. Fig. 4 demonstrates the performance of the VDR systems with and without the impedance model. The figure in the top shows that the maximum angular displacements are 1.2rad and 1.6rad for VDR system with and without the impedance model, respectively. The figure in the middle portrays the locomotion performance in displacement of two VDR systems. It can be clearly observed from these figures that within two motion cycles, the robot with impedance model has a superior performance (about 9cm in 13s) than the one without it (about 7cm in 13s). Besides, the performance of energy consumption is presented in the figure in the bottom for one motion cycle. The maximum input torques are 0.46N*m and 0.51N*m for VDR systems as shown in Fig. 6. Therefore, the energy consumed during a motion cycle can be calculated to 0.552J and 0.816J for VDR systems with and without the impedance, respectively. These results apparently demonstrate the effectiveness of the introduced impedance model.

B. Verification of the Desired Motion Generation

To verify the performance of the desired motion generation approach, comparative studies are performed with [18] (here referred to as EPC system), in which a two-stage velocity trajectory is designed using a conventional approach with heuristically chosen control parameters. The control scheme in Eq. (13) is employed to make convenient comparison. Based on the proposed motion generation approach, the parameters for the constructed trajectory in Eq. (2) and the trajectory in [18] are detailed in Table III.

TABLE III. Trajectory Parameters for Simulation

Trajectories	Time duration distributions (s)						
	t_1	t_2	t_3	t_4	t_5	t_6	t_7
Trajectory EPC	0.1	0.33	0.9	1.4	5.8	6.6	NA
Trajectory (2)	0.133	0.195	0.275	0.9	1.7	5.8	6.6

Simulation results are presented in Figs. 5-7. A zoom-in figure is affiliated in Fig. 5 to demonstrate the performance in the locomotion stage. It can be clearly observed from Fig. 5 that the maximum angular velocity using the proposed scheme is about 7.8 rad/s, which is lower than the EPC system

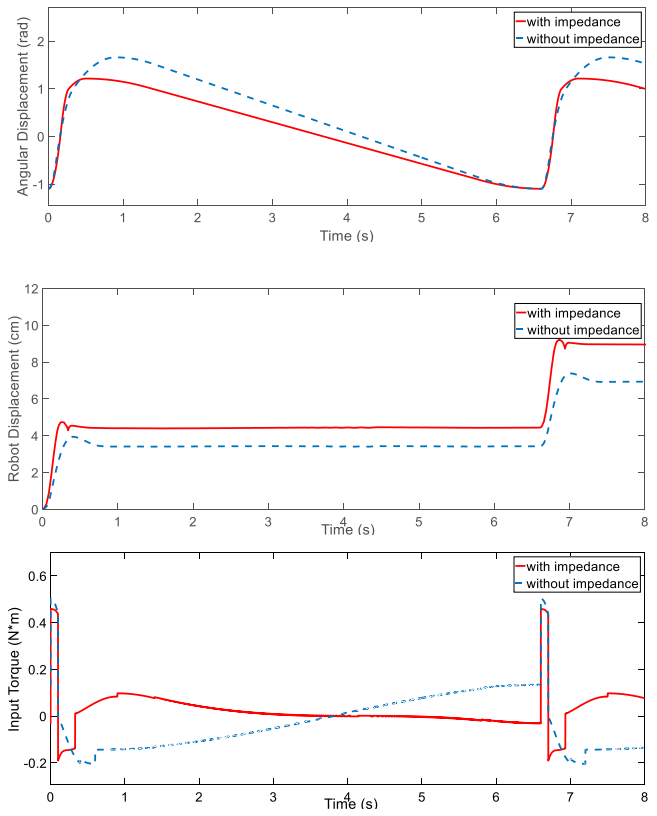

Fig. 4. Performance of the VDR systems with and without the impedance model (the VDR systems are tested in 8s).

with 11 rad/s. The proposed trajectory model presents a better transient performance in terms of overshooting that the maximum pendulum swing is about 68.75° (17.1° smaller than that of the EPC system). Simulation results have a good agreement with motion planning indexes and design choices.

The average velocity with the proposed trajectory model calculated from Fig. 6 for the first five cycles is 0.642cm/s, whereas it is 0.629cm/s for the EPC system. The transition functions inserted into locomotion stage guarantee the smooth transition and thereafter a lower maximum input torques as shown in Fig. 7 (0.5367 Nm compared with 0.6246 Nm of EPC system). This directly demonstrates a superior performance in energy efficiency. The backward motions are sufficiently counteracted as can be seen from Fig. 6. The results conclude that the friction-induced stick-slip motions are efficiently controlled through the proposed trajectory model, as such, the superior performances are guaranteed.

VII. Experimental Evaluation

The objective of the experiment here is to demonstrate and validate the proposed trajectory generation approach and its effectiveness. In the experiment, parameters of the VDR system are listed as follows: mass of the platform is 0.523kg, mass of the pendulum is 0.119kg, and length of the pendulum is 0.145m. According to the design choice (i), the pendulum is initialized at a fixed angle and travels afterwards with an anti-clockwise locomotion.

Figs. 8 and 9 present comparison of the experimental with the simulation results. From the figures, it is clearly observed that the pendulum moves in a certain range and the platform

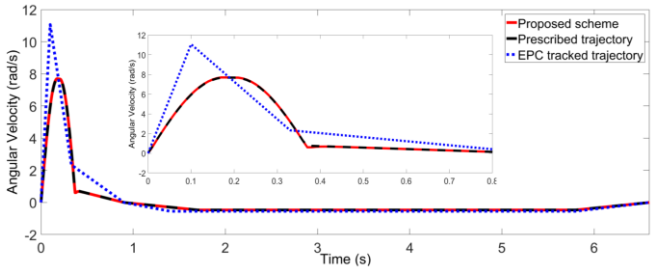

Fig. 5. Performance in trajectory tracking for one motion cycle.

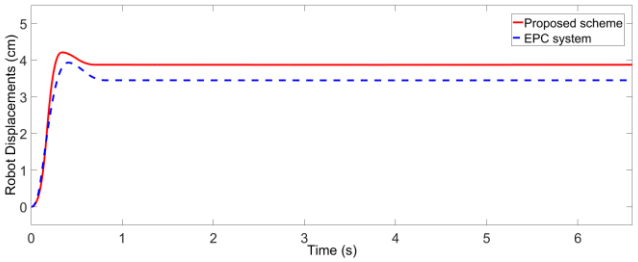

Fig. 6. Performance in displacement of VDR systems for one motion cycle.

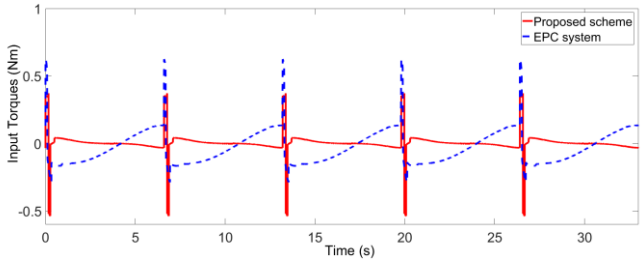

Fig. 7. Performance in control input torque of VDR systems for five cycles.

travels about 19.8cm during five motion cycles. It is shown in the figure that although there is a slight discrepancy between the results, motion pattern of the VDR system accurately follows the designed locomotion model. Besides, our experimental study also demonstrates that, displacements of the pendulum and the platform experience slight delay as well comparing to the simulated ones. From Fig. 9, we can see that the platform experiences a delay of about 2s after five motion cycles in the experiments than in the desired and simulation results. Nevertheless, the experimental trajectories demonstrate accurate motion patterns as the desired and simulation trajectories.

To make a vivid demonstration, we present some impressions of the pure locomotion and locomotion-restoring motion processes of the VDR system in our real-world experiments in the accompanying video[1]. Here, a sequence of snapshots of the self-propelled motion on the VDR system is presented in Fig. 10. The moving pendulum is marked with a red arrow in each snapshot. As captured from snapshots, the system is propelled over a surface rectilinearly through the interaction between the driving pendulum and the horizontal sliding friction, resulting into an alternative motion of sticking and slipping. Motion of the VDR system starts in a static state, and it moves when the magnitude of the resultant force applied maximal value of friction force. As marked in these snapshots, the platform moves a certain distance towards our left-hand direction after several motion cycles.

[1] Available in the attached video demo.

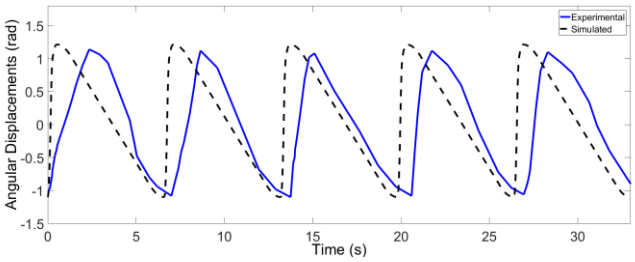

Fig. 8. Comparison of angular displacement of the driving pendulum.

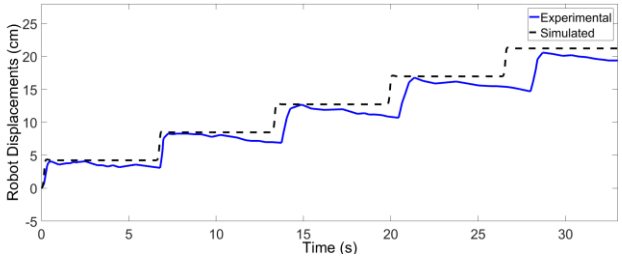

Fig. 9. Comparison of displacement of the platform.

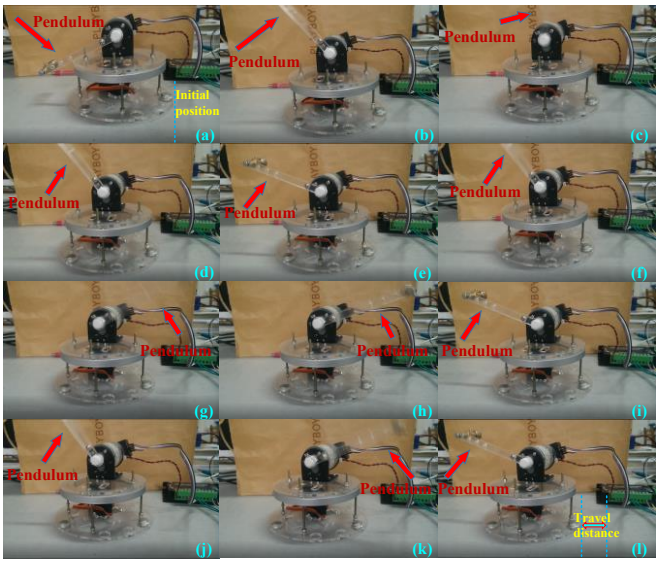

Fig. 10. Sequence of snapshots of the self-propelled VDR motions.

VIII. Conclusions

This paper undertook the issue of energy-efficient design and motion control for an underactuated VDR system. An analytical motion trajectory profile has been proposed and constructed to efficiently control the stick-slip motions of the VDR system with an optimality in unidirectional progression and energy efficiency. The satisfactions of both collocated and non-collocated constraint conditions are guaranteed. By doing so, dynamics of the actuated pendulum subsystem is reshaped to indirectly control the forward motion of the passive platform subsystem. Tracking control scheme has been designed through partially linearizing the system dynamics. The validity and effectiveness of the proposed robotic model and motion generation approach have been demonstrated using comparative simulation and experimental studies. In future work, several aspects will be emphasized: (i) Optimization of user designed parameters (e.g, critical boundaries of the trajectory and controller gains) by implementing some learning algorithms. (ii) Identification of system parameters (e.g., coefficients of the elasticity and viscosity) and dynamic friction. (iii) Real-time robot position feedback and evaluation of the computational complexity.

References

[1] K. Wang, G. Yan, G. Ma, and D. Ye, "An Earthworm-Like Robotic Endoscope System for Human Intestine: Design, Analysis, and Experiment," *Ann. Biomed. Eng.*, vol. 37, no. 1, pp. 210–221, Nov. 2008.

[2] H. M. Kim *et al.*, "Active locomotion of a paddling-based capsule endoscope in an in vitro and in vivo experiment (with videos)," *Gastrointest. Endosc.*, vol. 72, no. 2, pp. 381–387, Aug. 2010.

[3] G. Ciuti, P. Valdastri, A. Menciassi, and P. Dario, "Robotic magnetic steering and locomotion of capsule endoscope for diagnostic and surgical endoluminal procedures," *Robotica*, vol. 28, no. Special Issue 02, pp. 199–207, Mar. 2010.

[4] S. Yim, E. Gultepe, D. H. Gracias, and M. Sitti, "Biopsy using a Magnetic Capsule Endoscope Carrying, Releasing, and Retrieving Untethered Microgrippers," *IEEE Trans. Biomed. Eng.*, vol. 61, no. 2, pp. 513–521, Feb. 2014.

[5] P. Liu, H. Yu, and S. Cang, "Modelling and dynamic analysis of underactuated capsule systems with friction-induced hysteresis," in *Intelligent Robots and Systems (IROS), 2016 IEEE/RSJ International Conference on*, 2016, pp. 549–554.

[6] H. Fang and J. Xu, "Stick-Slip Effect in a Vibration-Driven System With Dry Friction: Sliding Bifurcations and Optimization," *J. Appl. Mech.*, vol. 81, no. 5, pp. 051001–051001, Dec. 2013.

[7] F. L. Chernous'ko, "Analysis and optimization of the rectilinear motion of a two-body system," *J. Appl. Math. Mech.*, vol. 75, no. 5, pp. 493–500, 2011.

[8] M. N. Huda and H. Yu, "Trajectory tracking control of an underactuated capsubot," *Auton. Robots*, vol. 39, no. 2, pp. 183–198, Aug. 2015.

[9] H. Fang and J. Xu, "Dynamics of a mobile system with an internal acceleration-controlled mass in a resistive medium," *J. Sound Vib.*, vol. 330, no. 16, pp. 4002–4018, Aug. 2011.

[10] M. T. Ravichandran and A. D. Mahindrakar, "Robust stabilization of a class of underactuated mechanical systems using time scaling and Lyapunov redesign," *IEEE Trans. Ind. Electron.*, vol. 58, no. 9, pp. 4299–4313, 2011.

[11] A. S. Shiriaev, L. B. Freidovich, and M. W. Spong, "Controlled invariants and trajectory planning for underactuated mechanical systems," *IEEE Trans. Autom. Control*, vol. 59, no. 9, pp. 2555–2561, 2014.

[12] V. Böhm and K. Zimmermann, "Vibration-driven mobile robots based on single actuated tensegrity structures," in *2013 IEEE International Conference on Robotics and Automation*, 2013, pp. 5475–5480.

[13] H. Yu, M. N. Huda, and S. O. Wane, "A novel acceleration profile for the motion control of capsubots," in *Robotics and Automation (ICRA), 2011 IEEE International Conference on*, 2011, pp. 2437–2442.

[14] H. Yu, Y. Liu, and T. Yang, "Closed-loop tracking control of a pendulum-driven cart-pole underactuated system," *Proc. Inst. Mech. Eng. Part J. Syst. Control Eng.*, vol. 222, no. 2, pp. 109–125, 2008.

[15] P. Liu, H. Yu, and S. Cang, "Geometric analysis-based trajectory planning and control for underactuated capsule systems with viscoelastic property," *Trans. Inst. Meas. Control*, p. 0142331217708833, Sep. 2017.

[16] P. Liu, H. Yu, and S. Cang, "On periodically pendulum-diven systems for underactuated locomotion: A viscoelastic jointed model," in *2015 21st International Conference on Automation and Computing (ICAC)*, 2015, pp. 1–6.

[17] H. Li, K. Furuta, and F. L. Chernousko, "Motion generation of the capsubot using internal force and static friction," in *Proceedings of the 45th IEEE Conference on Decision and Control*, 2006, pp. 6575–6580.

[18] P. Liu, H. Yu, and S. Cang, "Modelling and control of an elastically joint-actuated cart-pole underactuated system," in *Automation and Computing (ICAC), 2014 20th International Conference on*, 2014, pp. 26–31.